

Nonequilibrium Anion Detection in Solid-Contact Ion-Selective Electrodes

Ryan C. Gettler,^{||} Shima Mehregan,^{||} Henry D. Koenig, Andie M. Kaess, and Matthias J. Young^{*†}Cite This: *ACS Omega* 2024, 9, 16443–16457

Read Online

ACCESS |



Metrics & More

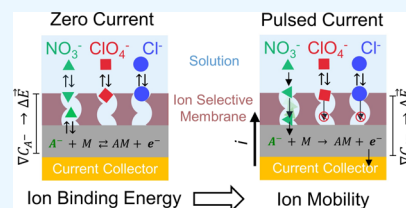


Article Recommendations



Supporting Information

ABSTRACT: Low-cost and portable nitrate and phosphate sensors are needed to improve farming efficiency and reduce environmental and economic impact arising from the release of these nutrients into waterways. Ion selective electrodes (ISEs) could provide a convenient platform for detecting nitrate and phosphate, but existing ionophore-based nitrate and phosphate selective membrane layers used in ISEs are high cost, and ISEs using these membrane layers suffer from long equilibration time, reference potential drift, and poor selectivity. In this work, we demonstrate that constant current operation overcomes these shortcomings for ionophore-based anion-selective ISEs through a qualitatively different response mechanism arising from differences in ion mobility rather than differences in ion binding thermodynamics. We develop a theoretical treatment of phase boundary potential and ion diffusion that allows for quantitative prediction of electrode response under applied current. We also demonstrate that under pulsed current operation, we can create functional solid-contact ISEs using lower-cost molecularly imprinted polymers (MIPs). MIP-based nitrate sensors provide comparable selectivity against chloride to costlier ionophore-based sensors and exhibit >100,000 times higher selectivity against perchlorate. Likewise, MIP-based solid contact ion-selective electrode phosphate sensors operated under pulsed current provide competitive selectivity against chloride, nitrate, perchlorate, and carbonate anions. The theoretical treatment and conceptual demonstration of pulsed-current ISE operation we report will inform the development of new materials for membrane layers in ISEs based on differences in ion mobility and will allow for improved ISE sensor designs.



1. INTRODUCTION

An excess of bioavailable nutrients in the form of nitrates and phosphates can pose serious ecological and human health concerns. Agricultural runoff is a primary source of these nutrients, leaching soluble nitrate and phosphate ions into aquatic ecosystems and drinking water resources. Accumulation of these pollutants can cause environmental degradation such as freshwater eutrophication and terrestrial health hazards like methemoglobinemia. Nutrient distributions can vary widely within a small geographical area and over short time frames.¹ Additionally, fertilizers can suffer from supply shortages and price volatility, making their economic use of considerable importance.^{2–4} To inform regulatory action and improve efficiency, knowledge of local real-time ion concentrations is necessary. Ion-selective electrodes (ISEs) are an attractive tool for the measurement of aqueous ion activities due to their ease of use, commercial accessibility, and high-throughput capability compared to more advanced laboratory techniques like ion chromatography. Solid contact ion-selective electrodes (SC-ISEs) are particularly interesting, as they are more easily configured for specialized applications and have been successfully demonstrated as nutrient sensors in soils,⁵ drinking water,⁶ and agricultural wastewater.⁷

In general, ISEs require an ion selective membrane (ISM) layer that provides selectivity toward a target ion. To this end, organic macromolecules known as ionophores have been developed which selectively bind specific ions and can be

incorporated into ISM polymer layers to provide selectivity.⁸ This ionophore approach has been especially successful for developing cation selective sensors due in part to a sound theoretical understanding of metal–ligand interactions and metal coordination chemistry, allowing the geometry and type of ligand interactions in an ionophore to be rationally designed for a target cation.^{9–12} In contrast, metal coordination chemistry does not provide the same degree of benefit for designing anion-centric ionophores, and correspondingly, fewer anion selective ionophore molecules are available, and these can be costly and exhibit variable results. For example, at the time of writing, nitrate ionophore VI (NIVI) costs around \$10,000 per gram from commercial suppliers, and some reports question its efficacy.¹³ These challenges motivate the (re)consideration of fundamental ISE theory and device design to identify potential opportunities to improve ISE sensors for anion detection.

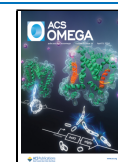
In conventional (also called passive, open-circuit, or zero-current) SC-ISE measurements, the electrode potential is

Received: January 4, 2024

Revised: March 8, 2024

Accepted: March 15, 2024

Published: March 30, 2024



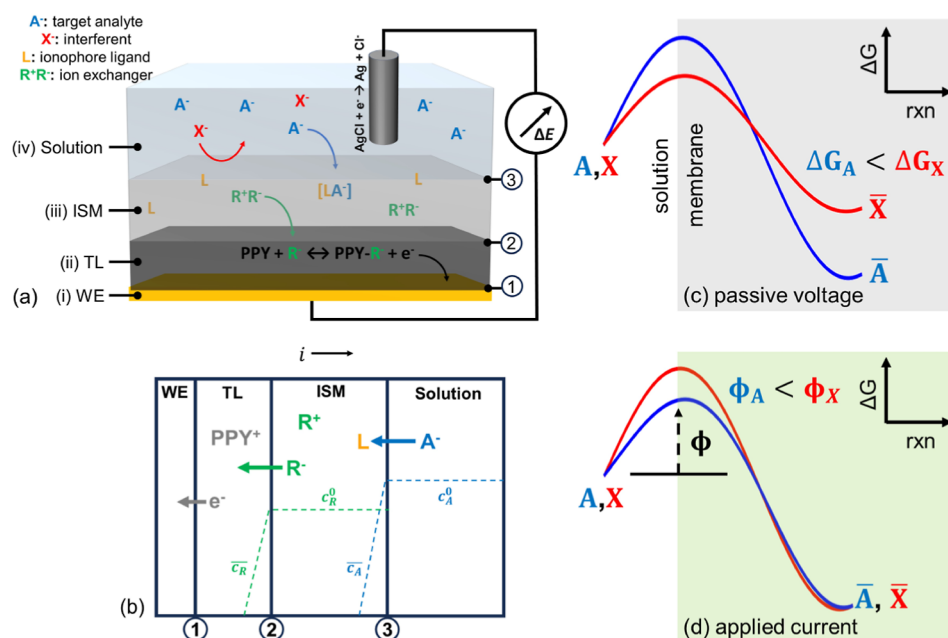


Figure 1. Schematic of (a) pulsed current ISE design and working principle including (i) working electrode (WE), (ii) transduction layer (TL), and (iii) ISM in contact with (iv) solution, corresponding to (b) electrode cross-section showing changes at phase boundaries 1–3, and reaction diagrams for migration of target *A* and interferent *X* under (c) zero-current potentiometry in a traditional ISE, where free energy (ΔG) dictates response, and (d) applied current conditions in an ion conducting film, where overpotential (ϕ) influences the analytical signal.

monitored relative to a reference electrode (RE) with no electrical input signal. Here, the equilibrium between the ions in the solution and membrane phases results in an interfacial charge separation and gives rise to a potential difference. This potential difference can be related to the solution phase ion activity via the Nernst equation, provided that the membrane activity is constant. In conventional ISEs, the sensor response time and sensitivity are governed by the equilibration time for mass transfer and ion insertion thermodynamics, respectively. Accordingly, long equilibration times, reference potential drift, and spontaneous membrane discharge can limit ISE performance.^{14–17} Additionally, interpretation of the electrode response curves is limited to the Nernst equation, and small deviations from the Nernstian predictions can cast doubt surrounding the processes dictating the measurement.^{18,19} Response characteristics are largely dictated by membrane thickness; that is, sensitivity over larger concentration ranges is achieved by increasing the amount of membrane material. Thicker membranes limit the effects of spontaneous membrane discharge, and thus provide higher sensitivities and detection ranges compared to thinner membranes,^{20,21} with typical membrane thicknesses ranging from 200 to 500 μm .^{13,20,22,23} However, because membrane components (especially ionophores) can be quite expensive, the use of large quantities of material to make these thicker membranes is undesirable. Although thinner membranes would reduce material costs, these thinner films do not provide Nernstian responses in conventional ISE measurements.

To enable the use of thinner membrane materials in ISEs, a number of nonequilibrium measurement techniques have been suggested as alternatives to open-circuit measurements. In contrast to conventional ISE measurements, nonequilibrium (also called active or instrumentally controlled) techniques influence the phase boundary activities via application of an external electrical signal. These nonequilibrium ion activity measurements can take many forms, each offering unique

advantages over zero-current measurement. Voltammetric and coulometric techniques are such alternatives in which the ISE is perturbed by the application of a potential cycle or step, and the resulting current–potential relationships are related to ion-transfer processes occurring in the system during perturbation. Analysis by voltammetry is inherently complicated, however, as artifacts like charging currents, voltage drops, and redox potential shifts must be accounted for when correlating ion activity and the acquired signal.^{23–26} While more tenable than voltammetry in terms of data analysis, coulometry suffers from exceptionally long response times (often several minutes per concentration) and large current drifts, making reliable measurement difficult to achieve and requiring additional hardware to correct.^{18,19,27,28} As such, application of these techniques to ISEs is somewhat impractical. Galvanostatic (constant or pulsed current) polarization of the ISE is perhaps the most attractive of the many nonequilibrium techniques, as data analysis is similar (or in some cases identical) to that of zero-current potentiometry. Experimentally, the detection limits of ISEs can be greatly extended without adjusting the device design by directly compensating membrane discharge with the applied current.^{22,29} Similar studies have shown improvements in potential stability and response time compared to zero-current measurements using the same electrodes.^{30–32} While these previous studies have demonstrated the practical benefits of using an input electrical signal to improve sensor performance, these “active” measurements have been largely limited to cation sensors (with some notable exceptions^{29–31}), and the studies employing galvanostatic measurement have not established quantitative mathematical models for phase boundary potential under constant current to reveal design principles to engineer new materials for “active” ISE measurement.

In this work, we report three advances in this field: (1) we report a SC sensor construction for nonequilibrium measurement of anions in an ISE geometry that provides benefits over

traditional passive ISE electrode designs including (a) allowing for thinner ISM layers and (b) removing the need for a stable RE by removing potential drift; (2) we modify established mathematical models describing phase boundary potential in ISEs to capture the effect of applied current and quantitatively predict ISE potential response under applied current; and (3) we describe how together this sensor construction and theoretical model description inform the design of anion sensors using ISE membrane layers that operate on differences in ion mobility through the membrane rather than on differences in ion binding energy from the solution into the membrane.

The salient principles of the cell concept described in this work are outlined in Figure 1. The electrode geometry we employ is a three-layer construction consisting of a bottom electrically conductive WE underlayer (Figure 1a.i), a middle TL that electrochemically converts anionic current to electronic current (Figure 1a.ii), and a top ISM layer (Figure 1a.iii) that exhibits selective transport of certain anions over others, controlling the types of anions that flow from the solution (Figure 1a.iv) through to the TL. The TL is a redox-active material that undergoes anion-mediated redox chemistry, such as polypyrrole (PPy), 3,4-poly(ethylenedioxythiophene) (PEDOT), or polyaniline (PANI). In this work, we use a PPy TL due to its ease of synthesis and rapid anion exchange properties. While the electrode construction shown in Figure 1a could also be used to perform measurements under passive conditions, the ability to force ions across the junctions using nonequilibrium techniques allows for adjustments of sensitivity and selectivity based on differences in transport. The physics governing nonequilibrium electrode charging are more complex than for conventional (passive) operation. For anion detection, a positive current is used to oxidize the TL, causing a counteranion R^- to cross the TL/ISM interface (boundary 2 in Figure 1b). To balance the charge, the target anion A^- crosses the ISM/solution interface (boundary 3 in Figure 1b), leading to the development of a measurable phase boundary potential. In the case of plastic ionophore-based membranes used in passive measurement conditions, selectivity to the target A^- over the interferent X^- is determined by a combination of transport kinetics and binding thermodynamics of the ion–ionophore ($[LA^-]$) complexes (Figure 1c). As indicated by Figure 1d, the ability to influence the interfacial ion transport via an electronic input signal enables the use of ISMs that exhibit differences in ion mobility even if these ions exhibit equivalent ion binding thermodynamics. In this work, we demonstrate this mode of sensor operation using plasticized PVC membrane responses with quantitative prediction of responses. This mode of operation allows for simplified electrochemical cell configurations and alternative membrane formulations for selective anion sensing.

2. EXPERIMENTAL SECTION

2.1. Electrochemical Measurements. Electrochemical processes were conducted on a Biologic SP-150 potentiostat, and data acquisition was done using the EC-LAB software package. A standard three-electrode setup was used, with a 6 mm graphite rod (99.9995%, Alfa Aesar) counter electrode and Ag/AgCl (SSC) RE (BASi). Polarization curves were obtained by a minimum of 10 repeat cycles of galvanostatic charging for 1 s followed by potentiostatic discharge at 0.0 V versus SSC for 10 s. Nitrate was spiked in increasing

concentration under stirring, and the process was repeated. Activity coefficients were calculated according to the Debye–Huckel or Davies formalism, as indicated in the main text. Selectivity coefficients were determined using the separate solution method, where coefficients were calculated using the slopes of the response curves when possible or estimated from the difference in potential at the highest tested activity when the slopes differ greatly.

2.2. ISE Fabrication. Three different ISM formulations were used in this work: (1) conventional ionophore-based nitrate ISMs, (2) molecularly imprinted nitrate ISMs, and (3) molecularly imprinted phosphate ISMs.

Polyvinyl chloride (PVC)-based ionophore ISEs were constructed using gold-coated plastic interdigitated working electrodes (IDEs, Metrohm, P-IDEAU50) due to the facile adhesion of PVC onto these plastic IDEs. PPy films were electrodeposited onto IDEs at a constant potential of 0.8 V for 30 min in an electrolyte of 0.1 M aqueous pyrrole (98%, Alfa Aesar) with 0.1 M NaNO_3 support electrolyte under continuous UHP argon purge (Airgas). The resulting films were rinsed with methanol (99.8%, Sigma-Aldrich) to remove unreacted monomers and dried at 50 °C for 10 min to evaporate excess methanol. After PPy electrodeposition, the ISM layer was applied. Conventional ionophore-based nitrate ISM layers were prepared by dissolving NIVI (NIVI, 5.2 wt %), dibutyl phthalate plasticizer (47.1 wt %), tetraoctylammonium chloride (0.6 wt %), and polyvinyl chloride (47.1 wt %) in excess THF. A 30 μL aliquot of the ISM cocktail was pipetted onto the electrode surface, making sure to completely cover the PPy TL. These were then dried in an oven at 50 °C for 10 min to remove THF and weighed on a 5-digit precision balance. Average ISM weights based on three electrodes was 2.4 mg, corresponding to a ~ 2 μm ISM thickness. This standard NIVI ISM formulation was used unless otherwise noted as a means to benchmark the measurement concept outlined in Figure 1.

Molecularly imprinted nitrate and phosphate ISEs employed gold-coated AT-cut quartz crystals (QZ, 5 MHz, Phillip Technologies) as the working electrodes. Electrochemical deposition of PPy was carried out at a constant potential of 0.8 V for 2 min in an electrolyte of 0.1 M aqueous pyrrole with 0.1 M NaNO_3 support electrolyte, under continuous UHP argon purge (Airgas) to deposit a layer of PPy onto the gold surface of the QZ substrates. Here, only 2 min of electrodeposition was required due to the rapid growth of PPy onto the gold surface of the QZ substrates. Molecularly imprinted ISMs were prepared using methods established previously.^{33,34} Briefly, 100 mmol 1-allyl-2-thiourea (98%, Sigma-Aldrich) was employed as the functional monomer, with 10.0 mmol isoamyl nitrate (98%, TCI) employed as the template molecule for nitrate imprinting and 10.0 mmol diphenyl phosphate (99%, Sigma-Aldrich) employed as the template molecule for phosphate imprinting. The imprinting polymerization reaction was performed by applying 100 mmol ethylene glycol dimethacrylate (98%, Sigma-Aldrich) as the backbone polymer to form a network of functional monomers and 1.2 mmol azobis(isobutyronitrile) (98%, Sigma-Aldrich) as the radical initiator in 4 mL of acetonitrile (99.9%, Fisher) as the solvent. To synthesize the polymer, each reaction mixture (containing either nitrate or phosphate template molecules) was prepared using the above material quantities and placed in an oven at a temperature of 55 °C for 16 h. This was followed by a heating step at 80 °C for an additional 3 h. The resulting polymers

were then processed by grinding and sieving. Then, to remove the template molecules, the polymer particles underwent a series of washing steps. Initially, a solvent mixture of 500 mL of methanol and triethylamine in a 4:1 ratio (v/v) was used, followed by subsequent soaking in pure methanol for 24 h. Finally, to construct the ISEs, a mixture of 25 mg of imprinted polymer particles and 20 mg of commercial silicone-based epoxy was adhered to the surface of the PPy layer formed on a gold QZ electrode. Nonimprinted polymers (i.e., polymers synthesized without a template) have been previously shown to have negligible nitrate³⁴ and phosphate³³ uptake and were not considered in this work. Control experiments (not shown) for the epoxy resin without the molecularly imprinted polymers (MIPs) did not show selectivity toward any of the anions tested below, making it a viable support material for the MIPs. We note, however, that as the epoxy resin cures, all ion transport through the epoxy slows and prevents ISE function. As such, these epoxy-resin supported MIP ISE sensors are only functional for ~ 3 days, and the data reported for the below sensors was collected within the first 48 h after sensor fabrication. The use of support polymers other than epoxy-resin will be the focus of future work.

3. THEORY

3.1. Potential Response in Current Polarized Plasticized PVC Membranes. Several theoretical treatments of nonequilibrium potentiometry have been previously presented^{22,31,32,35,36} and form the basis of the technique presented here. A formal relationship between current, time, and ion activities for polymeric membranes and MIPs is derived as follows.

In a mixed ion system, the total flux J due to an applied current i is given by eq 1.

$$J = \frac{i}{FA} \sum_j \frac{1}{z_j} \quad (1)$$

Here, z_j is the valence of ion j , F is the Faraday constant, and A is the active electrode area. Assuming negligible contributions from migration and convection terms, the transient flux of ion j is given by Fick's second Law, which, expressed in terms of concentration is

$$\frac{\partial c_j}{\partial t} = D_j \frac{\partial^2 c_j}{\partial x^2} \quad (2)$$

where x is the spatial domain in 1D, t is the elapsed time, and D_j is the diffusion coefficient of species j . The concentration as a function of position and time can be obtained by a Laplace transform of eq 2, setting the solution/membrane phase boundary at $x = 0$, and inverse transform to the time domain (see Bard et al. for a complete solution).³⁶

$$c_{j(0,t)} = c_j^0 - \frac{2i}{z_j FA} \sqrt{\frac{t}{\pi D_j}} \quad (3)$$

$$\bar{c}_{j(0,t)} = \bar{c}_j^0 + \frac{2i}{z_j FA} \sqrt{\frac{t}{\pi D_j}} \quad (4)$$

Here, the accent indicates a membrane phase property, and variables with no accent represent solution phase properties. The potential at the phase boundary due to these concentration distributions is given by^{22,31,32,35}

$$E_j - E_j^0 = \frac{RT}{z_j F} \ln \frac{k_j a_j}{\bar{a}_j} \quad (5)$$

Here, a_j and \bar{a}_j are the solution and membrane phase activities of ion j , respectively, E_j^0 is the standard cell potential, and k_j is the partition coefficient related to the free energy of solvation.

$$k_j = \exp\left(-\frac{\bar{\mu}^0 - \mu^0}{RT}\right) \quad (6)$$

To get eq 5 in terms of i and t , we need an expression for the membrane activity in terms of the membrane, ionophore, and ion exchanger concentrations. This is accomplished by a mass balance for the ionophore, where L_T is the total ionophore concentration in the membrane, \bar{c}_L is the concentration of free ionophore, and \bar{c}_{jL} is the concentration of the ionophore complexed with ion j .

$$L_T = \bar{c}_L + \sum_j \bar{c}_{jL} \quad (7)$$

We also need a charge balance over the membrane, given by eq 8.

$$z_R R_T + \sum_j (z_j \bar{c}_{jL} + z_j \bar{c}_j) = 0 \quad (8)$$

Here, z_R and R_T are the charge and concentration of the lipophilic ion exchanger salt. We now introduce the ligand/ion formation constant β_j as

$$\beta_j = \frac{\bar{c}_{jL}}{\bar{c}_j \bar{c}_L} \quad (9)$$

And place into eq 8 to get

$$z_R R_T + \sum_j z_j \bar{c}_j (1 + \bar{c}_L \beta_j) = 0 \quad (10)$$

Now consider the case of a binary system with target analyte A and interferent ion X , for which eq 10 is

$$z_R R_T + z_A \bar{c}_A (1 + \bar{c}_L \beta_A) + z_X \bar{c}_X (1 + \bar{c}_L \beta_X) = 0 \quad (11)$$

Equation 11 can be rearranged to give

$$\frac{z_A \bar{c}_A (1 + \bar{c}_L \beta_A)}{\bar{\gamma}_A} \left[1 + \frac{z_X \bar{\gamma}_A \bar{a}_X (1 + \bar{c}_L \beta_X)}{z_A \bar{\gamma}_X \bar{a}_A (1 + \bar{c}_L \beta_A)} \right] = -z_R R_T \quad (12)$$

Here, concentrations were replaced by activities with the corresponding coefficients $\bar{\gamma}$. Rearranging eq 5, we can rewrite eq 12 in terms of the standard cell potential for species A and X .

$$\frac{\bar{a}_A (1 + \bar{c}_L \beta_A)}{\bar{\gamma}_A} \left[1 + \frac{z_X \bar{\gamma}_A a_X k_X e^{-z_X E_X^0 / s} (1 + \bar{c}_L \beta_X)}{z_A \bar{\gamma}_X a_A k_A e^{-z_X E_A^0 / s} (1 + \bar{c}_L \beta_A)} \right] = \frac{R_T}{|z_A|} \quad (13)$$

Here, we have used the fact that for a monovalent ion/exchanger pair, $z_R = -|z_j|$, and $s = RT/F$. We can now use the definition of the Nikolsky selectivity coefficient $K_{A,X}$ to rewrite eq 13.^{35,37,38} For the case $z_A = z_X$, we have

$$\frac{\bar{a}_A(1 + \bar{c}_L\beta_A)}{\bar{\gamma}_A} \left[1 + \frac{\bar{\gamma}_A a_X}{\bar{\gamma}_X a_A} K_{A,X} \right] = \frac{R_T}{|z_A|} \quad (14)$$

Assuming the membrane activity coefficients are unity, the membrane activity of target *A* is then

$$\frac{1}{\bar{a}_A} = \frac{|z_A|(1 + \bar{c}_L\beta_A)}{a_A R_T} \left[a_A + a_X K_{A,X} \right] \quad (15)$$

Because the free ionophore concentration is generally not known, it is convenient to rewrite eq 15 in terms of *i* and *t*. Assuming all the ions in the membrane exist in the complexed form, we can write eq 7 as

$$\begin{aligned} L_T &= \bar{c}_L + \bar{c}_{AL} + \bar{c}_{XL} \\ &= \bar{c}_L + \bar{c}_A^0 + \frac{2i}{z_A F A} \sqrt{\frac{t}{\pi D_A}} + \bar{c}_X^0 + \frac{2i}{z_X F A} \sqrt{\frac{t}{\pi D_X}} \end{aligned} \quad (16)$$

Here, \bar{c}_{AL} and \bar{c}_{XL} are the concentrations of ion–ionophore complexes with target *A* and interferent *X*, respectively. It should be noted that if the ionophore is consumed during polarization such that free ions are being pulled into the membrane, binding affinity will no longer influence electrode response, and selectivity will be dictated by ion transport. Assuming the diffusion coefficients in the membrane are equal and the initial membrane concentrations are zero, eq 16 reduces to

$$\bar{c}_L = L_T - \frac{4i}{z_A F A} \sqrt{\frac{t}{\pi D}} \quad (17)$$

We can define the second term in eq 17 as

$$\bar{N} \equiv \frac{4i}{z_A F A} \sqrt{\frac{t}{\pi D}} \quad (18)$$

Eqs. 17 and 18 can be inserted into eq 5 to give the full description of the potential at the solution/membrane interface.

$$\begin{aligned} E_{(a_A,i,t)} &= \frac{s}{z_A} \ln\{a_A + a_X K_{A,X}\} \\ &+ \frac{s}{z_A} \ln\left\{ \frac{|z_A| k_A}{R_T} [1 + (L_T - \bar{N})\beta_A] \right\} \end{aligned} \quad (19)$$

Note here that a_A , a_X , and $K_{A,X}$ are all functions of *i* and *t* according to Eqns. 3, 13 and 14. The phase boundary potential at the CP/membrane interface must also be considered and is given by

$$E_{CP} = \frac{RT}{z_{CP} F} \ln \frac{k_{CP} a_{CP}}{\bar{a}_{CP}} \quad (20)$$

Here, all values retain their previous meanings, and the CP subscript denotes the conductive polymer dopant ion. Given that the dopant concentration in the polymer phase is very high (6 M), such that $a_{CP} \gg \bar{a}_{CP}$, and we can treat a_{CP} as constant.²² The charge balance at this interface is

$$z_R R_T + z_{CP} \bar{c}_{CP} (1 + \bar{c}_L \beta_{CP}) = 0 \quad (21)$$

for which the membrane activity due to polarization is

$$\frac{1}{\bar{a}_{CP}} = \frac{|z_{CP}| (1 + \bar{c}_L \beta_{CP})}{\bar{\gamma}_{CP} R_T} \quad (22)$$

For the case where the CP dopant ion and analyte ion *A* are the same, eq 22 can be rewritten as

$$\frac{1}{\bar{a}_A} = \frac{|z_A| (1 + \bar{c}_L \beta_A)}{R_T} \quad (23)$$

and inserted into eq 19 to give the full phase boundary description

$$\begin{aligned} E_{(a_A,i,t)} &= \frac{s}{z_A} \ln\{a_A + a_X K_{A,X}\} \\ &+ \frac{s}{z_A} \ln\left\{ |z_A|^2 a_{CP} k_A k_{CP} \left[\frac{1 + (L_T - \bar{N})\beta_A}{R_T} \right]^2 \right\} \end{aligned} \quad (24)$$

The second term in eq 24 is constant at a given current and time. Additionally, the measured potential will be influenced by the voltage drop from uncompensated resistance (ΔV) over the ISE system and the baseline (open-circuit or stripping) potential E_b as follows.

$$\Delta V + E_b = i R_{eq} + \frac{it}{C_{eq}} + E_b \quad (25)$$

Here, R_{eq} and C_{eq} are the equivalent resistance and interfacial capacitance, respectively. Given the high capacitance of the CP layer, small input currents, and short pulse width, the voltage drop over the capacitor (second term on the right side of Eqn. 23) should be negligible.^{22,30} Adding Eqns. 24 and 25 and defining

$$\phi \equiv E_{(a_A,i,t)} - E_b \quad (26)$$

we get our final expression for the total measured voltage, where $B_{(i,t)}$ contains the membrane components and electronic voltage drop.

$$\phi_{(a_A,i,t)} = \frac{s}{z_A} \ln[a_A + \sum_Y K_{A,X} a_X] + B_{(i,t)} \quad (27)$$

where E is the reported potential, E_b is the baseline (stripping) potential, R is the gas constant, F is Faraday's constant, z_A and a_A are the valency of and activity of analyte *A*, a_X is the activity of interferent *X*, $K_{A,X}$ is the selectivity coefficient, and $B_{(i,t)}$ is an offset parameter. A demonstration of the ability of eq 27 to describe the potential response of a NIVI electrode under pulsed current at varying ion activities in the presence of interferents is provided in Supporting Information, Section 1. Note that eq 27 is analogous to the Nikolsky equation for open-circuit potential measurements of mixed solutions of monovalent ions. The measured potential relative to the baseline is thus expected to have response curves similar to those obtained by zero-current potentiometry, provided $B_{(i,t)}$ is constant during measurement conditions. We expect $B_{(i,t)}$ to be a constant if membrane activity and voltage drop are fixed at a given current and time. For example, the value of $B_{(i,t)}$ at a fixed value of current and time across multiple NIVI electrodes and electrolyte conditions is found to be a constant value of -24 ± 8 mV. In other words, in order to obtain a reversible electrode response under applied current conditions, spontaneous discharging of the membrane must be compensated by the charging process (i.e., the membrane activity must be approximately constant). In this context, several noteworthy differences between pulsed current and passive voltage measurements merit discussion. First, if the magnitude and/

or duration of the applied current are too short under active measurement, significant polarization of the membrane may not occur, leading to negligible changes in response. Conversely, if the magnitude and duration of the applied current are large under active measurement, the solution/ISM junction can be drained of ions, leading to dielectric potential drop arising from the depletion region and producing a hyper-Nernstian response. This can be largely addressed by using an ionic strength adjuster (i.e., adding a background salt to the measurement solution to ensure the boundary layer is not depleted); however, hyper-Nernstian behavior can still occur if significant migration potentials develop in the membrane during charging.^{39,40} While common in potentiometric laboratory measurements, ionic strength adjustment is not always practical, e.g., for field use. In this situation, the current and/or time can be adjusted to prevent phase boundary depletion according to eq 3 by setting $c_{j(0,t)} = 0$ to estimate the limiting conditions. We emphasize that this may require additional experimental optimization and, possibly, longer acquisition times. Second, the choice of a stripping potential is somewhat arbitrary, and standard nonpolarizable reference electrodes can be replaced with polarizable electrodes provided the RE is overcapacitive compared to the ISE. Finally, the selectivity of the membrane is strongly influenced by the rate of transport across the solution/ISM interface,⁴¹ and the selectivity coefficient is expected to fluctuate with current and/or time. This fact implies that active measurement employs a fundamentally different approach to ion sensing compared to traditional ISE measurements in which ion transport limitations can take precedence over binding affinity of target analytes to active sites, as outlined in Figure 1d above.

3.2. Potential Response in Current Polarized MIP Membranes. For ion conducting membranes containing no ion exchanger and immobilized active sites, ions must traverse the length of the membrane to complete the circuit during polarization. This will lead to the development of an internal diffusion–migration potential, and the flux must be rewritten to include this effect.^{35,38,39}

$$J = -D \frac{d\bar{c}}{dx} + \mu\bar{c} \frac{d\varphi}{dx} \quad (28)$$

Here, μ is the ion mobility ($\text{m}^2 \text{V}^{-1} \text{s}^{-1}$), φ is the diffusion–migration potential, and the other terms retain their previous definitions. Equation 28 can be rearranged to give

$$\frac{d\varphi}{dx} = -\frac{J}{\mu\bar{c}} + \frac{D}{\mu\bar{c}} \frac{d\bar{c}}{dx} \quad (29)$$

Equation 29 can be integrated over the total membrane thickness d to give the potential difference due to diffusion–migration process

$$\int_0^d d\varphi = -\frac{J}{\mu} \int_0^d \frac{dx}{\bar{c}} + \frac{D}{\mu} \int_0^d d \ln \bar{c} \quad (30)$$

for which the partial solution is

$$\varphi = -\frac{J}{\mu} \int_0^d \frac{dx}{\bar{c}} - \frac{D}{\mu} \ln \left[\frac{\bar{c}(0)}{\bar{c}(d)} \right] \quad (31)$$

Note that eq 31 can be solved by inserting an appropriate test function for the concentration. Here, we use the Henderson equation^{35,38}

$$\bar{c}_{(x)} = \bar{c}_{(0)} + \frac{\bar{c}_{(d)} - \bar{c}_{(0)}}{d} x \quad (32)$$

a commonly used linear equation for determining junction potentials; however, the diffusion/migration potential is given by the difference at the end points of the integration, and for qualitative purposes the exact functional form is arbitrary. We can multiply eq 32 through by membrane activity coefficients $\bar{\gamma}$ and insert it into eq 31 and use the substitution $u = \bar{a}_{(x)}$, and $\frac{du}{dx} = \frac{\bar{a}_{(d)} - \bar{a}_{(0)}}{d}$ to get

$$\varphi = \frac{Jd}{\mu[\bar{a}_{(d)} - \bar{a}_{(0)}]} \int_{\bar{a}_{(0)}}^{\bar{a}_{(d)}} \frac{du}{u} + \frac{D}{\mu} \ln \left[\frac{\bar{a}_{(0)}}{\bar{a}_{(d)}} \right] \quad (33)$$

for which the solution is just

$$\varphi = \left\{ \frac{RT}{zF} - \frac{id}{\mu zFA[\bar{a}_{(d)} - \bar{a}_{(0)}]} \right\} \ln \left[\frac{\bar{a}_{(0)}}{\bar{a}_{(d)}} \right] \quad (34)$$

Here, we have used eq 1 for J and $D/\mu = RT/zF$. While the exact functional form of \bar{c} is not known, the activity at position $x = d$ can be estimated from eq 4 by setting $\bar{a}^0 = 0$ and using the Einstein diffusion length $d \approx \sqrt{2Dt}$.

$$\bar{a}_{(d)} = \frac{2\bar{\gamma}id}{\sqrt{2\pi zFAD}} \quad (35)$$

To observe a Nernstian response, the membrane activity at $x = 0$ ($\bar{a}_{(0)}$) must be proportional to the solution phase activity $\bar{a}_{(0)}$, $\bar{a}_{(d)}$ must be a constant, mobility μ must be sufficiently large, and the condition $\bar{a}_{(0)} > \bar{a}_{(x)}$ must hold for all x . Given these criteria, the membrane phase boundary concentration can be estimated by combining Eqns. 3 and 4 to get

$$\bar{a}_{(0)} = a^0 - \frac{2\gamma i}{zFA} \sqrt{\frac{t}{\pi D}} + \bar{a}_{(d)} \quad (36)$$

As for the plasticized PVC membranes, a baseline potential and voltage drop will be present according to eq 23, and our final expression is

$$\begin{aligned} \phi &= \varphi_{(a_A, i, x)} - E_b \\ &= \left\{ \frac{RT}{z_A F} - \frac{ix}{\mu_A z_A FA[\bar{a}_{A(x)} - \bar{a}_{A(0)}]} \right\} \ln[\bar{a}_{A(0)}] + B_{(i)} \end{aligned} \quad (37)$$

Here, as before, $B_{(i)}$ contains the voltage drop and constant phase boundary terms, and $\bar{a}_{A(0)}$ is a function of current.

4. RESULTS AND DISCUSSION

As a test case to examine the above theoretical treatment and demonstrate the benefits of pulsed current nonequilibrium ISE measurement for anion sensors, we employed a thin-film NIVI membrane for nitrate detection, as described in the Experimental Section. Here, we employed a PPy TL to absorb the anions under a positive electrical potential (oxidation), as depicted in Figure 1a. To obtain reproducible ϕ versus t curves, the measurement (charge) step must be followed immediately by regeneration (discharge) step to return the TL to a reduced state. This process can take several minutes under zero-current conditions,^{40,42} and we instead opt for controlled discharging at a fixed reducing (or stripping) potential of 0.0 V (approximately 200 mV more reducing than the equilibrium potential of oxidized Ppy). Figure 2a–d shows sample raw data

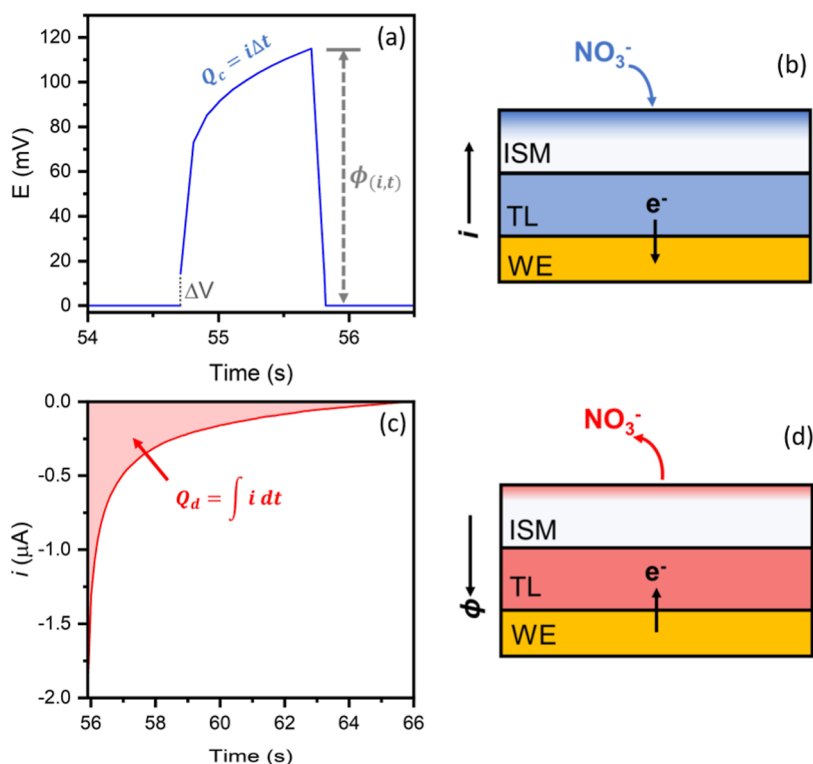


Figure 2. Potential/time dependence (a) and schematic of membrane loading (b) of a thin-film NIVI ISM during galvanostatic charging, where Q_c is the accumulated charge and ϕ is the potential shift from the stripping potential (0.0 V vs SSC) taken as the analytical signal. The current decay (c) and membrane discharge process (d) are shown for the stripping step, where Q_d is the removed charged.

curves and physical schematics of typical charging and discharging experiment. Here, the active current measurement consists of two steps: (1) a single pulse of constant current measurement for 1 s, where the shift in potential versus OCV is tracked during the duration of the measurement, and the overpotential (ϕ) is calculated at the end of this constant current pulse (Figure 2a,b), and (2) a potential hold at 0.0 V versus SSC for 10 s to return the PPy TL to a reduced state (Figure 2c,d).

The reversibility of a given charge/discharge cycle can be assessed by calculating the total charge Q transferred during the forward and reverse processes, where Q is directly related to the moles of charge by the Faraday constant F . For the sample data in Figure 2a–b, we calculate a ratio Q_c/Q_d of $0.98(\pm 0.04)$ based on five repeat cycles, indicating that ions extracted by a 1 s current pulse are adequately removed by a 10 s discharge at constant voltage. Depending on the choice of material for the transducing layer, the stripping potential used during the regeneration step can impact potential drift.³⁰ This is due to large changes in conductivity associated with different redox forms of conductive polymers that can lead to large voltage drops and irreproducible measurements. For the polypyrrole transducer employed here, the onset potential for oxidation is roughly -100 mV versus SSC,⁴³ and stripping potentials around this value (here, we use 0 mV vs SSC) are appropriate for regenerating the PPy TL between measurements. We note that over-reduction of PPy may lead to a decrease in the electrical conductivity of PPy that could impede electronic measurements.

To validate the theoretical treatment presented in eq 27, we compare model and experimental response curves in Figure 3. Here, several variables related to the geometry and physical

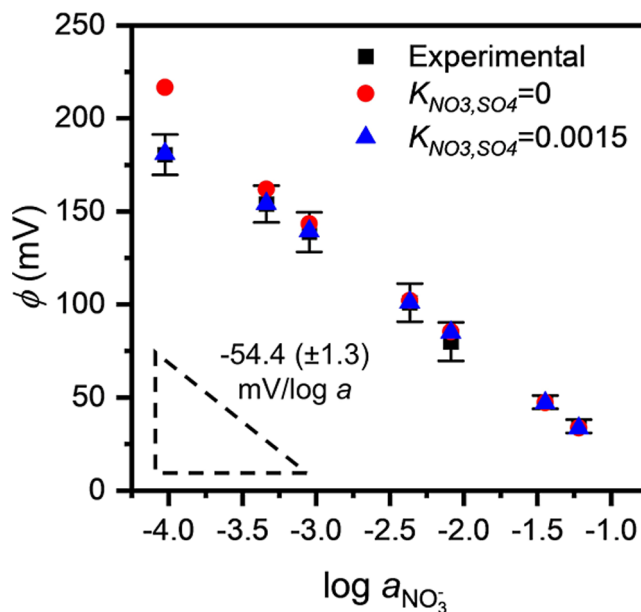


Figure 3. Comparison of experimental (black) and predicted (red and blue) nitrate response curves using a thin-film NIVI ISM at an applied current of $2 \mu\text{A}$ for 1 s with a 0.01 M Na_2SO_4 ionic strength adjuster. Error bars are representative of two repeat measurements (10 charge–discharge cycles each) at each concentration. Sensitivity S is given by the slope of the experimental curve.

properties of the electrode must be known to model the electrode response. The detailed treatment for how these variables are related to eq 27 is provided in detail in Section 3.1. Values that could not be calculated were either measured directly or estimated from the literature and are as follows: $D =$

10^{-5} cm²/s,⁴⁴ $\bar{D} = 10^{-7}$ cm²/s,⁴⁴ $R_T = 3$ μ mol/cm³, $L_T = 30$ μ mol/cm³, $\beta_{\text{NO}_3} = 1.4$,¹³ $k_{\text{NO}_3} = 0.00015$,⁴⁵ $k_{\text{CP}} = 15$,⁴⁶ $\Delta V = 20$ mV, $A = 0.17$ cm², $a_{\text{CP}} = 6$ mmol/cm³,²² and $T = 300$ K. Here, D and \bar{D} are the solution phase and membrane phase diffusion coefficients, respectively, based on molecular dynamics simulations of chloride anions in bulk solution and polymer membranes. R_T and L_T refer to the ion exchanger and ionophore concentration, respectively, and are calculated based on the percent composition of the membrane, average membrane weight, and estimated membrane density (1.1 g/cm³).⁴⁷ The binding constant β_{NO_3} was obtained from the sandwich membrane method.¹³ The partition coefficients for nitrate anions in the membrane (k_{NO_3}) and conductive polymer phase (k_{CP}) were taken from solubility measurements in plasticizer and polypyrrole media. The voltage drop arising from uncompensated resistance ΔV was measured from the polarization curves as indicated in Figure 2a, and the active area A was determined from the line width and spacing of the interdigitated electrode current collectors. The conductive polymer phase activity a_{CP} was estimated from the density and average doping level of electropolymerized PPy. Activities in Figure 3 were calculated by using the Debye–Huckel equation. The model behavior agrees well with experimental data at intermediate to high activity ranges ($10^{-3.3}$ – 10^{-1}), with major deviation occurring at low ion activity. We note that the model predictions in Figure 3 assumed a selectivity coefficient of $K_{\text{NO}_3,\text{SO}_4} = 0$ for this calculation (i.e., no SO_4^{2-} transport through the membrane). However, some coextraction of the sulfate anion likely occurs at low nitrate activity and would explain the depression of the experimental value below the predicted value. Setting $K_{\text{NO}_3,\text{SO}_4} = 0.0015$ provides the exact agreement of the model with the experimental data at $a_{\text{NO}_3} = 10^{-4}$.

As described in the introduction, the response characteristics of ISEs under passive conditions are largely influenced by membrane composition, with thinner membranes showing lower sensitivity and detection ranges.²¹ Indeed, the nitrate ISE sensors used here which employed a thin ~ 2 μ m NIVI ISM (>100 times thinner than typical NIVI ISM layers) show poor response and long equilibration times under zero-current potentiometry. Figure 4a shows changes in the open-circuit potential with time as the nitrate activity is increased. While the electrodes do respond to changes in activity as suggested surrounding the discussion of Figure 1, the sensitivity (-24 mV/decade) is $<50\%$ of the Nernstian slope, and measurements can take several minutes to stabilize. These characteristics are inherent to potentiometric measurements using thin-membrane SC-ISEs, for which no membrane discharge compensation mechanism exists, and response metrics are often poor compared to liquid-contact analogues.^{48,49}

In contrast, the applied current method offers several significantly improved performance metrics in comparison to those of open-circuit potentiometry. Figure 4b shows the results of galvanostatic polarization of the same electrode over the same activity range shown in Figure 4a, where the lines plotted for each indicated activity represent 10 consecutive pulsed current measurement cycles. The data in Figure 4b indicate that instrumental control of the electrode system allows for a drastic reduction in equilibration time. Defining the equilibration time as the time needed for the potential drift to stabilize within 1 mV/min following each activity increase, we calculate an average equilibration time of 174 s (2.9 min) for the passive measurements in Figure 4a compared to 10 s

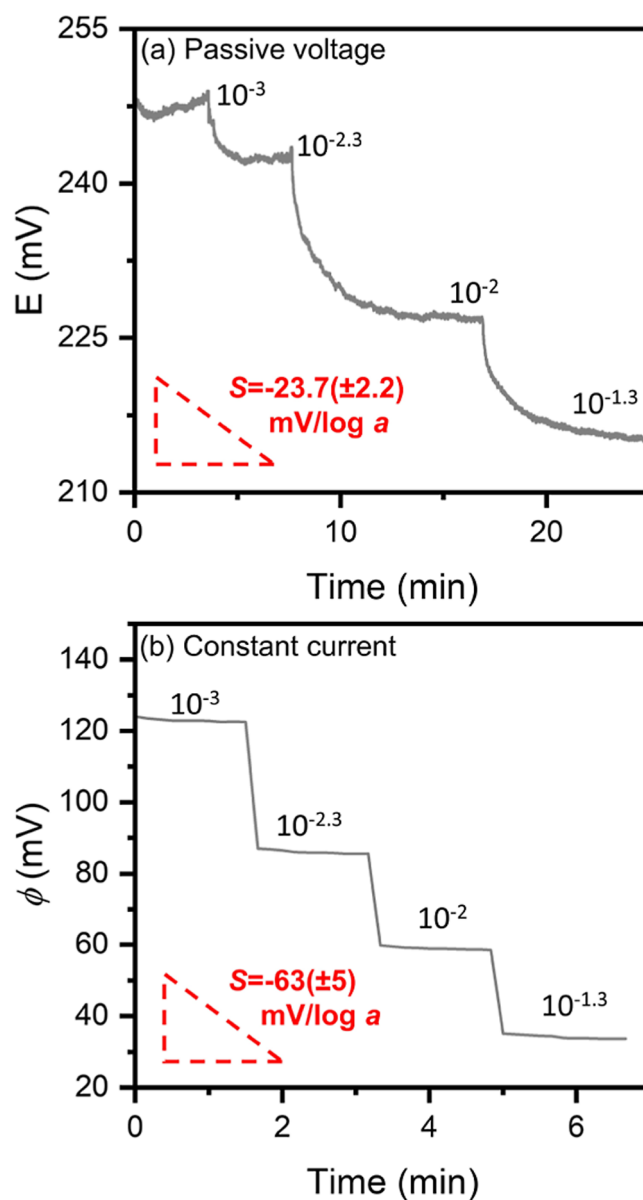


Figure 4. Variation in potential with time for (a) a thin-film NIVI ISM electrode under open-circuit conditions and (b) the same electrode under 2 μ A applied current, where the lines under each concentration in (b) are representative of 10 charge/discharge cycles at each concentration. Approximate activities corresponding to the potential step are indicated at each step. Sensitivity S is shown for each condition in red.

using the galvanostatic measurement in Figure 4b. This is especially crucial in long-term studies or continuous monitoring applications where large fluctuations in potential could compromise measurements. Moreover, pulsed current detection facilitates faster response times by driving the ion flux at the solution/ISM interface, enabling the >10 -fold decrease in equilibration times between Figure 4a,b. This is particularly advantageous in dynamic systems, where rapid changes in ion concentrations occur. Here, active pulsed current control is used to tune the ISE system such that membrane self-discharge is adequately compensated and the phase boundary activity is representative of the bulk.

Another advantage arises from the pulsed current measurement approach. Because the analytical signal employed here is

the differential potential measured relative to baseline as opposed to a standardized reference potential, ideal REs can be replaced with lower-cost alternatives. High capacitance materials undergo minimal potential shifting at low charging currents, and the resulting signal is dominated by changes at the WE.⁵⁰ This concept is shown in Figure 5, in which the

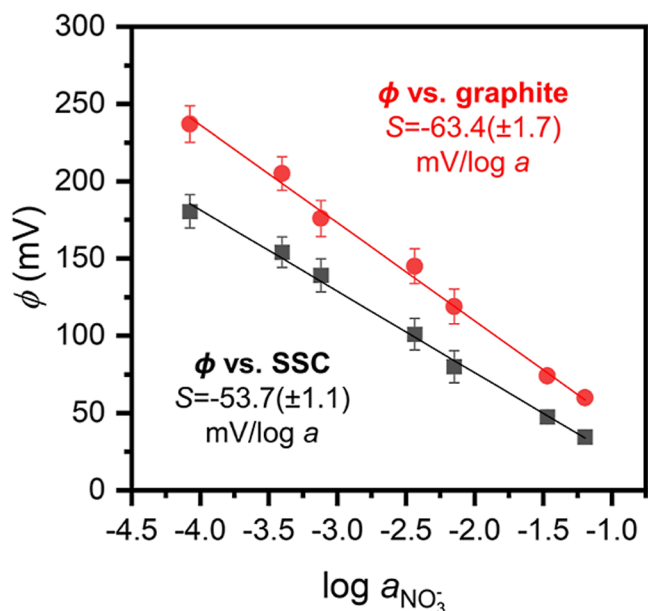


Figure 5. Comparison of nitrate calibration curves for a thin-film NIVI ISM using SSC (black) and graphite (red) RE. Calibration was done at 2 μA input signal and 1 s pulse width in 0.01 M Na_2SO_4 background electrolyte. Error bars are representative of two repeat measurements each.

nitrate response using a graphite rod as a RE is similar to that observed using an SSC reference. We emphasize the practical benefit indicated by the data presented in Figure 5, where the potential drift of the reference is inconsequential. This is because the measurement under active ISE measurement is of the overpotential during electrode charging (ϕ) over a short (~ 1 s) time scale, rather than the open circuit potential versus a reference over a longer time scale. Any drift in the reference potential is subtracted during the overpotential measurement using two pulsed current (measurement) and reducing potential (regeneration) steps (Figure 2). We note that a shift in calibration offset is expected when comparing measurements between SSC and graphite REs, as the uncompensated resistance will be different between these two reference electrodes with different geometries. Indeed, Figure 5 shows a 12 ± 4 mV change in offset between REs. This difference is constant at fixed current and time, however, and does not reduce the measurement sensitivity. The results in Figure 5 are interesting for several reasons. The ability to use overcapacitive REs allows for reduction in ISE complexity, eliminating associated issues like RE storage, electrolyte leakage, and potential drift. Additionally, simplified (e.g., carbon) RE materials allow for alternative configurations and geometries if the cumbersome liquid-contact RE can be eliminated. Lastly, standard reference electrodes (like SSC) are expensive, and replacement of these electrodes with cheaper constituents can significantly reduce the cost of ISE systems.

For the system and method employed here to be suitable for environmental analysis, the ISE should be able to resolve the

target anion in environmental samples. This can often be difficult, as intrinsic interferences, pH variation, and dissolved reactive species can cause substantial deviations from measurements in carefully controlled lab conditions.⁵¹ To test this, we measured the nitrate response of the polarized SCISEs in CERC 100 hardness water, a standardized representative of natural Missouri river water (water quality: dissolved oxygen = 8.2 mg/L, pH = 8.3, hardness = 109 mg/L CaCO_3 , alkalinity = 91 mg/L as CaCO_3).⁵² A more detailed analysis of CERC 100 hardness water chemistry can be found in ref 52. The results of the galvanostatic nitrate detection are shown in Figure 6. Similar to nitrate detection in 18 M Ω water (Figure 3), the curve is depressed at a low nitrate activity of $\sim 10^{-4}$, where interference from background ions is significant.

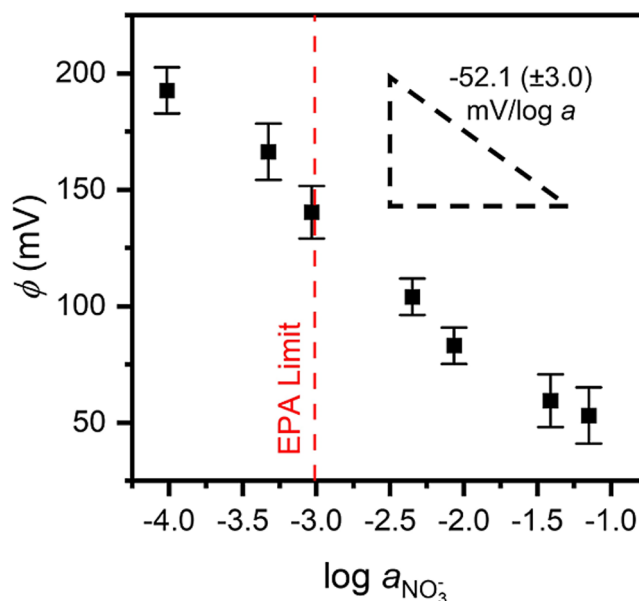


Figure 6. Nitrate detection using a thin-film NIVI ISM in CERC 100 hardness mock river water obtained at a 2 μA input current with a 0.01 M Na_2SO_4 ionic strength adjuster. Error bars are representative of two repeat measurements (10 charge/discharge cycles each) at each nitrate activity.

At nitrate activity $> 10^{-1.5}$ in Figure 6, the response is again depressed. This is likely due to saturation of the solution–membrane interface, which is not observed in the case of laboratory water samples (Figure 3) but is induced by the additional ions in the mock environmental samples. Regardless, the sensitive region of the current polarized electrodes encompasses the EPA maximum contamination level for nitrate (45 ppm),⁵³ indicated by the dashed red line on Figure 6.

In addition to response characteristics, the selectivity coefficient $K_{A,X}$ varies with current and time for ions with different lipophilicity.⁵⁴ Assuming eq 27 holds for all anion species X , the selectivity of the SC–ISE can be calculated using the separate solution method. Figure 7 shows the results of pulsed polarization in separate solutions, in which the selectivity improves with an increased current to a limiting average value of 0.002 on the 10–20 μA range. Unfortunately, depletion effects occur at these higher currents, and to avoid depletion, the current should be limited to the 2–4 μA range, for which we measure $K_{\text{NO}_3,\text{Cl}} = 0.02$. While the electrode response is excellent in this range, typical open-circuit $K_{\text{NO}_3,\text{Cl}}$

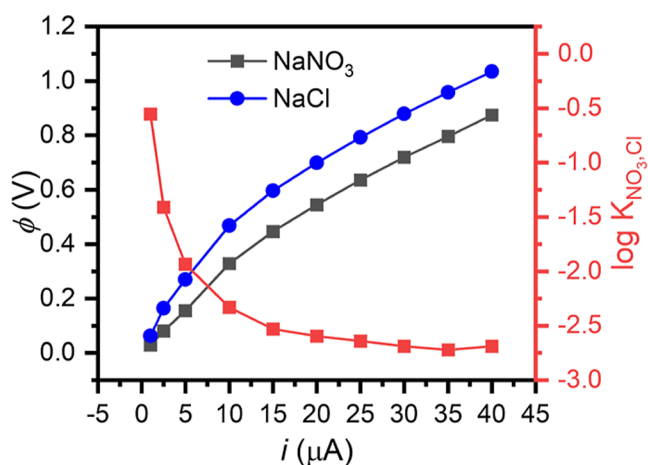


Figure 7. Polarization curves obtained in separate 0.01 M solutions of NaNO_3 (gray) and NaCl (blue) for a thin-film NIVI ISM electrode. The resulting selectivity factors as a function of current are shown in red and plotted on the right axis.

values for NIVI-containing ISM's range from 0.006 to 0.01¹³ depending on the methods involved. This indicates that some selectivity is sacrificed using the thin NIVI membranes with pulsed current measurement compared to the thick NIVI membranes with passive measurement. A more detailed theoretical and experimental description of the dependence of selectivity on current for solutions of mixed ions is given in Supporting Information, Section 2. We attribute this reduced selectivity of these NIVI-based ISEs under pulsed current operation to the fact that the applied polarization helps drive interfering ions through the membrane without the assistance of the ionophore or ion-exchange mechanisms.³¹ We note that the ionophore-based NIVI ISM formulation that we employ has been previously engineered for its ion binding affinity to nitrate, but this is not the operative property that governs selectivity in pulsed current operation, as outlined in Figure 1c,d.

In typical passive ISE operation, membrane selectivity is determined largely by the binding affinity among the target ion, the interfering ion, and the ionophore or active site. When an external electric field is employed, differences in ion transport become significant, allowing for the selective transport of target ions through the membrane. The use of applied current as a mechanism for selectivity based on differences in ion transport opens a new landscape of membrane designs. Materials with

inherently slower ion transport rates, previously deemed impractical, can now be used as ISE components. By using applied current to accelerate ion transport, these materials can potentially offer higher selectivity factors without compromising sensitivity and response time. This principle is illustrated in Figure 8, where ions having higher mobility will move through the membrane with higher flux, and will have higher concentrations in the membrane during polarization, and therefore a less drastic voltage shift during galvanostatic charging. In other words, it is differences in solid state diffusivity through the membrane that govern ion selectivity under the active current measurement. Solid state ion diffusivity through membranes is a kinetically limited process, arising from energy barriers for ion hopping through the solid, and is not governed by the thermodynamics of ion solubility in the membrane, as outlined in Figure 1d above, and repeated in Figure 8b.

This realization that the membrane selectivity under active measurement is governed by differences in ion transport kinetics rather than ion binding thermodynamics in the ISM has a meaningful impact on sensor design. Specifically, this means that materials need not necessarily be engineered to have favorable thermodynamics for binding a target anion to be useful as membrane materials in ISEs. Instead, if different ions experience different transport behaviors through a given material, this material can be used as a membrane material in an ISE sensor under pulsed current measurement. To test this conclusion, we replaced the NIVI ionophore membranes used above with a nitrate-templated ethylene glycol dimethacrylate and allyl thiourea (MIP-N) MIP membrane material. This MIP-N powder was blended within an epoxy suspension matrix and constructed into a PPy/MIP-N ISE according to the methods section. Briefly, allyl thiourea monomers serve as active sites for templating nitrate-selective sites into the MIP-N polymer based on hydrogen bonding interactions. These monomers are coordinated to an organo-nitrate (isoamyl nitrate, IAN) during synthesis, and cross-linked in place with polyethylene glycol dimethacrylate. The IAN is then removed, leaving nitrate-templated sites in the polymer. The polymer is suspended in an epoxy matrix and cast onto the PPy-coated gold surfaces of QZ electrodes. This type of MIP-N material has been shown to uptake nitrate ions by impedimetric³⁴ methods where enhanced mobility of the templated ion through the material was used to measure the nitrate concentration in test solutions. Based on the previous demonstrations that nitrate transport is enhanced in this MIP-

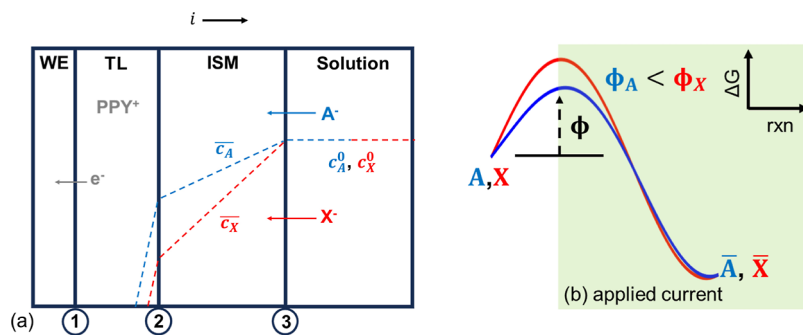


Figure 8. Electrode cross section showing an ion conducting membrane (a) templated for target anion A^- with increased flux for the target over interfering anions X^- during galvanostatic polarization and (b) differences in overpotential due to higher target concentration between phase boundaries 2 and 3.

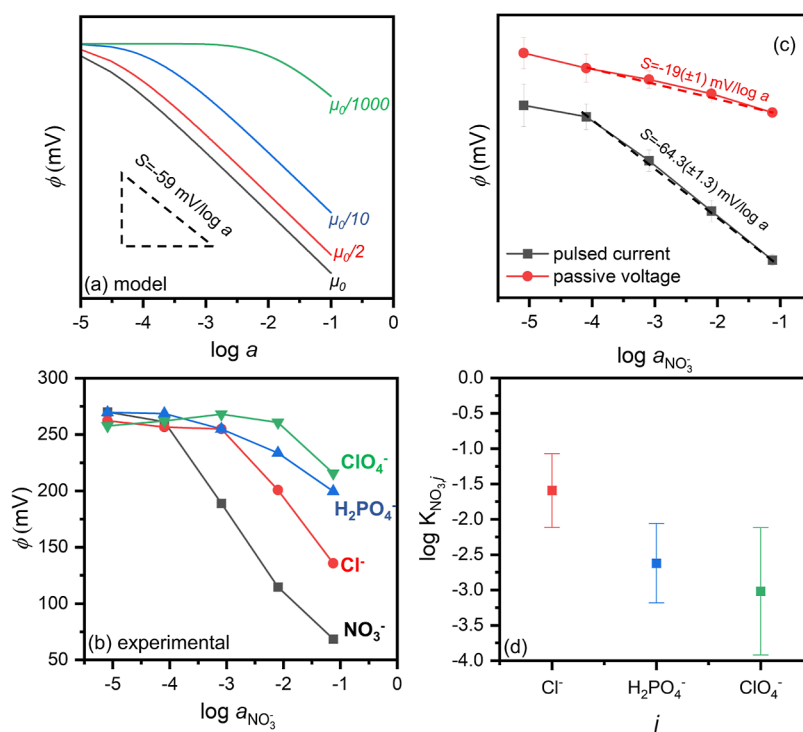


Figure 9. Theoretical (a) and experimental (b) response curves using MIP-N ISM sensors at $3 \mu\text{A}$ current with a 1 s pulse width in a 0.1 M Na_2SO_4 ionic strength adjuster, where the model mobilities in (a) are reported relative to the maximum value necessary to reproduce the experimental curves in (b). Panel (c) shows a comparison between nitrate response under open-circuit (red) and applied current (black) conditions. Selectivity factors showing preference of MIP-N sensors over chloride (red), phosphate (blue), and perchlorate (green) are shown in panel (d). The selectivity factor $K_{\text{NO}_3, \text{H}_2\text{PO}_4}$ was calculated by assuming all phosphate ions are in the -1 charge state. Error bars are representative of sample standard deviations for three electrodes with two measurements each.

N over other anions, we would expect these MIP-N membranes to also be functional in active ISE measurements. The MIP-N membranes have several distinctive differences from the plastic membranes discussed earlier. First, the cross-linked active sites are immobilized in an epoxy matrix, in contrast to the freely moving ionophore sites in a plastic membrane. Second, the MIP-N membranes do not contain an anion exchanger salt, and thus, the ion exchange mechanisms utilized by plastic membranes are not available. This means that MIP-N sensors operate by a different mechanism from the mechanism described in Figure 1, where ions must traverse the membrane during charging in order to maintain current flow, and the results of eq 27 must be modified to account for membrane diffusion and migration contributions. The final voltage response in this case is given by eq 37, where steady-state conditions were assumed for solving the Nernst–Planck equation. We note that higher currents are needed to sufficiently polarize the MIP-N sensors compared to the plastic membranes, and the concentration of the ionic strength adjuster was set to 0.1 M Na_2SO_4 to limit interfacial potential drops. As such, the Debye–Hückel treatment of activity is no longer appropriate, and all following activities were calculated using the Davies equation. It follows that for ions with high mobility, the second term in the curly brackets of eq 37 will be small, and a quasi-Nernstian response will be obtained. As the mobility decreases significantly, the second term in the curly brackets of eq 37 will become dominant, requiring a higher potential to sustain a specified current. Treating the transport of multiple ions across the membrane as a group of parallel resistors, the highest mobility ion will dominate the potential drop behavior for a given ISE operated under a pulsed current.

In Figure 9, we compare the model predictions from eq 37 versus the performance of ISMs fabricated using the MIP-N ISM. Figure 9a shows the qualitative prediction based on eq 37 for ϕ versus $\log(a)$ for ions with different mobilities. Here, qualitative predictions were used because the solubility and diffusivity of each ion in the composite membrane were unknown, and these are necessary for quantitative predictions. The responses using pulsed current measurement for different anions with a MIP-N ISE sensor in Figure 9b agree with these qualitative trends, indicating that $\mu_{\text{NO}_3^-} > \mu_{\text{Cl}^-} > \mu_{\text{H}_2\text{PO}_4^-} > \mu_{\text{ClO}_4^-}$ for MIP-N, where $\mu_{\text{ClO}_4^-} \cong \mu_{\text{NO}_3^-}/1000$. In Figure 9c, we plot the responses for nitrate using passive vs active measurements. Similar to the thin NIVI ISMs in Figure 3a above, the MIP-N membranes exhibit sub-Nernstian responses under passive voltage conditions, making it difficult to separate ion insertion processes from other surface charge contributions to the measured voltage. This response is greatly improved by utilizing the pulsed current method, with near-Nernstian responses to nitrate activity observed at the $3 \mu\text{A}$ input signal (Figure 9c). The depressed response curve for passive measurement in Figure 9c despite ISM thicknesses of more than hundreds of microns suggests that the nitrate-thiourea complexation constant for these membranes is low. Despite this weak complexation interactions, control of interfacial transport via applied current overcomes these inherent thermodynamic limitations, providing a near-Nernstian response under pulsed current measurement conditions.

As expected, the influence of transport phenomena on sensitivity extends to the selectivity for the MIP-N sensors as

well. This point is illustrated in Figure 9d, where a comparison of separate solution calibrations of the MIP-N sensors to nitrate analyte and chloride, monobasic phosphate, and perchlorate interferences is shown. These interferences were examined to test the effects of the ionic radius and geometry on selectivity. The nitrate and chloride anion have roughly the same radius (179 pm)⁵⁵ but planar and spherical geometry, respectively. Monobasic phosphate and perchlorate both have pyramid geometry, but significant differences in covalent radii (200 and 250 pm, respectively).⁵⁵ The MIP-N sensors show large overpotentials in the presence of these interferences when compared to those of nitrate. These overpotentials arise from the additional energy required to move the interfering ions through the MIP-N ISM, suggesting that the templating procedure indeed provides a coordination network that facilitates the transport of the nitrate ions. The larger interference effect of the Cl⁻ relative to ClO₄⁻ and H₂PO₄⁻ suggests that the source of ion selectivity in MIP-N may arise from size-exclusion effects.

The selectivity values in Figure 9d are comparable to commonly reported values for ionophore-based nitrate ISEs operated under zero-current potentiometry, except for the perchlorate response. The perchlorate anion is a major interferent for most nitrate ISEs due to the high binding constant of perchlorate to the nitrate ionophore.^{13,56} In contrast, the MIP-N sensors are highly discriminate against perchlorate ($K_{\text{NO}_3, \text{ClO}_4} = 0.001$ vs $K_{\text{NO}_3, \text{ClO}_4} = \sim 300$ for NIVI).^{13,56} This suggests a membrane network well templated for nitrate transport but ill-suited for transport of ions with different geometries. The advantage of such a transport-controlled sensor is that it offers a different mode of selectivity without the need for specialized ionophores, provided coordination environments and pathways can be introduced via an appropriate template molecule during membrane synthesis. Based on the proof-of-concept demonstration for MIP-N above, we expected that the templating procedure used to produce the MIP-N membranes could be extended to other species. To show this, we synthesized membranes using the same formulation as that in Figure 9, but replaced the isoamyl nitrate template with diphenyl phosphate to make phosphate templated sensors (MIP-P). Sensitivity and selectivity curves using the combined MIP-P sensors and galvanostatic detection are shown in Figure 10.

Unlike the plastic membrane and MIP-N sensors, the MIP-P sensors exhibit deviations from the Nernstian response described in eq 37 for both monobasic and dibasic forms of phosphate. Qualitatively, the response of the MIP-P sensors to monobasic phosphate is similar to that of the MIP-N sensors for nitrate; however, the slope of the linear region indicated in Figure 10 is hyper-Nernstian. As the background electrolyte activity is quite high, the hyper-Nernstian response is not likely the result of phase boundary depletion, and there are other more plausible explanations. Simultaneous coextraction of background electrolyte and analyte can lead to hyper-Nernstian behavior under passive conditions, and it is possible that this phenomenon is occurring during membrane charging.³⁷ For dibasic phosphate, there is a nonlinear region at low activity coupled with a hyper-Nernstian region at higher activity (note that for an ion of -2 charge, eq 27 predicts a response of -30 mV per decade). Interestingly, the potential response to dibasic phosphate is lower than that of monobasic phosphate by ~ 100 mV, indicating the preference of the MIP-P electrode for this ion form. The nonlinear trend for dibasic

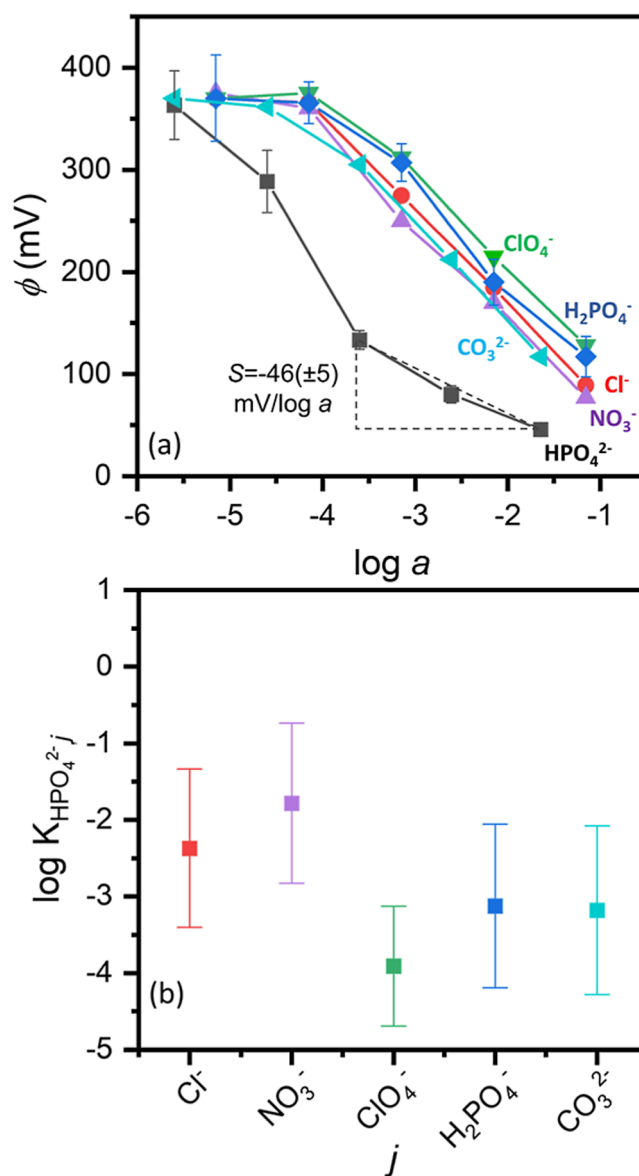


Figure 10. Response curve (a) of MIP-P ISM sensors to monobasic (blue) and dibasic (black) phosphate as well as other interferences using $3 \mu\text{A}$ applied current with a 1 s pulse width in a 0.1 M Na₂SO₄ ionic strength adjustor. Panel (b) shows selectivity factors estimated from panel (a). Error bars are representative of samples standard deviations from two electrodes with two measurements each.

phosphate in Figure 10 can be explained in terms of pH changes occurring in the test solution during analyte addition (see Supporting Information Section 2 for more detail). At low activity ($\sim 10^{-5}$), 80% of phosphate is in the monobasic form. As the activity of dibasic phosphate (black curve) is increased to 10^{-3} , the pH increases rapidly, dibasic phosphate becomes the dominant form, and a linear response is obtained beyond this point. The slope of the dibasic phosphate curve is approximately half that of monobasic phosphate, indicating transport of a -2 charged ion. In contrast, the monobasic form is dominant for all data points on the blue curve in Figure 10.

Similar to MIP-N sensors, the selectivity of MIP-P sensors was determined by separate solution calibration with nitrate, chloride, perchlorate, and carbonate (Figure 10b). Selectivity factors were calculated by eq 38.

$$\log K_{i,j} = \frac{z_i(\phi_j - \phi_i)}{S} + \log \frac{a_i}{a_j^{z_i/z_j}} \quad (38)$$

Here, i refers to dibasic phosphate (HPO_4^{2-}), j is the interferent, S is the slope indicated in Figure 10a, activities a_i and a_j were taken from the highest dibasic phosphate activity ($10^{-1.6}$), and potential ϕ_j was calculated at $\log a_j = -1.6$ by linear fits to each interferent curve. The MIP-P sensors show no selectivity to monobasic phosphate over the interfering ions, meaning that the templating procedure produced a highly nonspecific coordination environment for the monovalent form. The sensors do, however, show high selectivity for divalent phosphate, which suggests that the valency is influencing phosphate transport through the polymer matrix. We note that the diphenyl phosphate template molecule we employed during phosphate templating is expected to produce tetrahedral coordination of three R–P–O⋯H–N–R hydrogen bonding interactions (with isoamyl nitrate) and one R–P–O–H⋯O–R hydrogen bonding interaction (with ethylene glycol dimethacrylate) in the MIP formulation. The dibasic form of phosphate [$\text{P}(\text{OH})\text{O}_3^{2-}$] reflects the same quantity and type of hydrogen bonding interactions as expected for diphenyl phosphate, whereas the monobasic form [$\text{P}(\text{OH})_2\text{O}_2^-$] has a mismatch in the hydrogen bonding interaction types and quantities. The rejection of carbonate, another divalent anion, by the MIP-P electrodes may be explained by the different geometry (trigonal planar) and different quantity and type of intermolecular hydrogen bonding interactions relative to the template molecule. While further work is needed to confirm these theories regarding the molecular origins of these transport differences, the diphenyl phosphate template molecule has indeed imparted selectivity for transport of dibasic phosphate and, when coupled with pulsed current measurement, produces a functional ISE to detect phosphate.

5. CONCLUSIONS

In this work we demonstrate a predictive theoretical description and practical examples of pulsed current operation of ISEs for anion detection. Using PVC-based ISMs containing a nitrate ionophore (NIVI), we demonstrate that pulsed current provides the benefits of (1) > 100 times thinner ISE membrane layers, (2) > 10 times faster measurement, and (3) simpler construction without the need for a chemical RE. In addition to the demonstration of these practical benefits, we identify that the fundamental sensing mechanism during pulsed current measurement arises from differences in ion mobility in the ISM, rather than differences in thermodynamic binding affinity. The ability to use differences in mobility as the sensing mechanism under pulsed current operation allows for simpler materials to be used as ISM layers in ISEs. This motivated us to use established MIP membrane materials as ISM layers in pulsed-current ISE devices. We report successful ISE sensors for nitrate and phosphate using this approach. The MIP-based nitrate sensor design we report operated under pulsed current provides near-equivalent selectivity against chloride to ionophore-based sensors ($K_{\text{NO}_3,\text{Cl}} = 0.01$) and exhibits substantially higher selectivity against perchlorate compared to NIVI ($K_{\text{NO}_3,\text{ClO}_4} = 0.001$ vs $K_{\text{NO}_3,\text{ClO}_4} = \sim 300$ for NIVI). The MIP-based phosphate sensor design we report operated under pulsed current provides exceptional selectivity against Cl^- , NO_3^- , ClO_4^- , and CO_3^{2-} .

To develop improved pulsed-current anion ISE sensors, new materials are needed as ISM layers that exhibit differences in anion mobility, with the highest mobility for the target analyte. While MIPs are demonstrated in this work as one viable option to provide selective anion mobility, and represent a broader trend in sensors in general,^{57–59} one of the challenges with the MIP platform is the uniform delivery of a MIP membrane layer.⁶⁰ In this work, we overcome this challenge using a support polymer, but this support polymer poses practical issues for device design, requiring no ion interactions, high chemical stability, and strong electrode surface adhesion. One potential opportunity to overcome this design limitation is to form uniform, continuous MIP ISM layers directly onto the ISE sensor surface via, e.g., vapor-phase polymer deposition and/or cross-linking.^{43,61–63} Beyond the MIP platform, recent studies have provided new fundamental insights into differences in ion mobility in crystalline solids,⁶⁴ nanopores,^{65–67} and lead halide perovskites.⁶⁸ Leveraging this improved understanding of different anion mobilities in other material classes may allow new materials to be incorporated into pulsed-current ISE sensor designs to create new anion sensors.

■ ASSOCIATED CONTENT

Supporting Information

The Supporting Information is available free of charge at <https://pubs.acs.org/doi/10.1021/acsomega.4c00131>.

Comparison between theoretical and experimental predictions for polarized PVC electrode response in a mixed ion solution and considerations for pH variation in phosphate measurements (PDF)

■ AUTHOR INFORMATION

Corresponding Author

Matthias J. Young – Chemical and Biomedical Engineering, University of Missouri, Columbia, Missouri 65211, United States; Department of Chemistry and Materials Science and Engineering Institute, University of Missouri, Columbia, Missouri 65211, United States; orcid.org/0000-0001-7384-4333; Email: matthias.young@missouri.edu

Authors

Ryan C. Gettler – Chemical and Biomedical Engineering, University of Missouri, Columbia, Missouri 65211, United States

Shima Mehregan – Department of Chemistry, University of Missouri, Columbia, Missouri 65211, United States

Henry D. Koenig – Department of Chemistry, University of Missouri, Columbia, Missouri 65211, United States

Andie M. Kaess – Chemical and Biomedical Engineering, University of Missouri, Columbia, Missouri 65211, United States

Complete contact information is available at:

<https://pubs.acs.org/10.1021/acsomega.4c00131>

Author Contributions

^{||}R.C.G. and S.M. contributed equivalently.

Notes

The authors declare no competing financial interest.

■ ACKNOWLEDGMENTS

The authors acknowledge support from the United States Geological Survey Great Rivers Cooperative Ecosystems

Studies Unit through Award Number G21AC10446. A.K. acknowledges support for an REU from the National Science Foundation through award 2149721. H.D.K. acknowledges support from the Mizzou Forward Undergraduate Research Training Grant. M.J.Y. acknowledges support from the MU College of Engineering Incentive Funds program. We also thank Patrick Kinlen at the University of Missouri for useful advice and conversations.

REFERENCES

- (1) Li, Z.; Taylor, J.; Frewer, L.; Zhao, C.; Yang, G.; Li, Z.; Liu, Z.; Gaulton, R.; Wicks, D.; Mortimer, H.; Cheng, X.; Yu, C.; Sun, Z. A Comparative Review of the State and Advancement of Site-Specific Crop Management in the UK and China. *Front. Agric. Sci. Eng.* **2019**, *6*, 116.
- (2) Uçak, H.; Ari, Y.; Yelgen, E. The Volatility Connectedness among Fertilisers and Agricultural Crop Prices: Evidence from Selected Main Agricultural Products. *Agric. Econ.* **2022**, *68*, 348–360.
- (3) Lahmiri, S. Asymmetric and Persistent Responses in Price Volatility of Fertilizers through Stable and Unstable Periods. *Phys. A* **2017**, *466*, 405–414.
- (4) Kim, S.-W.; Brorsen, B. W. Forecasting Urea Prices. *Appl. Econ.* **2017**, *49*, 4970–4981.
- (5) Ali, M. A.; Wang, X.; Chen, Y.; Jiao, Y.; Mahal, N. K.; Moru, S.; Castellano, M. J.; Schnable, J. C.; Schnable, P. S.; Dong, L. Continuous Monitoring of Soil Nitrate Using a Miniature Sensor with Poly(3-Octyl-Thiophene) and Molybdenum Disulfide Nanocomposite. *ACS Appl. Mater. Interfaces* **2019**, *11*, 29195–29206.
- (6) Wardak, C.; Grabarczyk, M. Analytical Application of Solid Contact Ion-Selective Electrodes for Determination of Copper and Nitrate in Various Food Products and Drinking Water. *J. Environ. Sci. Health, Part B* **2016**, *51*, 519–524.
- (7) Patel, V.; Kruse, P.; Selvaganapathy, P. R. Review—Solid State Sensors for Phosphate Detection in Environmental and Medical Diagnostics. *J. Electrochem. Soc.* **2022**, *169*, 077505.
- (8) Bakker, E.; Bühlmann, P.; Pretsch, E. Polymer Membrane Ion-Selective Electrodes—What Are the Limits? *Electroanalysis* **1999**, *11*, 915–933.
- (9) Ishimatsu, R.; Izadyar, A.; Kabagambe, B.; Kim, Y.; Kim, J.; Amemiya, S. Electrochemical Mechanism of Ion-Ionophore Recognition at Plasticized Polymer Membrane/Water Interfaces. *J. Am. Chem. Soc.* **2011**, *133*, 16300–16308.
- (10) Yamada, K.; Deb, A.; Shoba, V. M.; Lim, D.; Maji, B.; Modell, A. E.; Choudhary, A. Rational Design of Silicon-Based Zinc Ionophores. *Angew. Chem., Int. Ed.* **2022**, *61*.
- (11) Bühlmann, P.; Pretsch, E.; Bakker, E. Carrier-Based Ion-Selective Electrodes and Bulk Optodes. 2. Ionophores for Potentiometric and Optical Sensors. *Chem. Rev.* **1998**, *98*, 1593–1688.
- (12) Johnson, R. D.; Bachas, L. G. Ionophore-Based Ion-Selective Potentiometric and Optical Sensors. *Anal. Bioanal. Chem.* **2003**, *376*, 328–341.
- (13) Damala, P.; Zdrachek, E.; Bakker, E. Commercially Available Nitrate Ionophores in Potentiometric Sensors Are Not Superior to Common Ion-exchangers. *Electroanalysis* **2023**, *35*.
- (14) Ivanova, N. M.; Levin, M. B.; Mikhelson, K. N. Problems and Prospects of Solid Contact Ion-Selective Electrodes with Ionophore-Based Membranes. *Russ. Chem. Bull.* **2012**, *61*, 926–936.
- (15) Maccà, C. Response Time of Ion-Selective Electrodes. *Anal. Chim. Acta* **2004**, *512*, 183–190.
- (16) Radu, A.; Radu, T.; McGraw, C.; Dillingham, P.; Anastasova-Ivanova, S.; Diamond, D. Ion Selective Electrodes in Environmental Analysis. *J. Serb. Chem. Soc.* **2013**, *78*, 1729–1761.
- (17) Sokalski, T.; Ceresa, A.; Fibbioli, M.; Zwickl, T.; Bakker, E.; Pretsch, E. Lowering the Detection Limit of Solvent Polymeric Ion-Selective Membrane Electrodes. 2. Influence of Composition of Sample and Internal Electrolyte Solution. *Anal. Chem.* **1999**, *71*, 1210–1214.
- (18) Wang, H.; Yuan, B.; Yin, T.; Qin, W. Alternative Coulometric Signal Readout Based on a Solid-Contact Ion-Selective Electrode for Detection of Nitrate. *Anal. Chim. Acta* **2020**, *1129*, 136–142.
- (19) Han, T.; Mattinen, U.; Bobacka, J. Improving the Sensitivity of Solid-Contact Ion-Selective Electrodes by Using Coulometric Signal Transduction. *ACS Sens.* **2019**, *4*, 900–906.
- (20) Szigeti, Z.; Vigassy, T.; Bakker, E.; Pretsch, E. Approaches to Improving the Lower Detection Limit of Polymeric Membrane Ion-Selective Electrodes. *Electroanalysis* **2006**, *18*, 1254–1265.
- (21) Sokalski, T.; Zwickl, T.; Bakker, E.; Pretsch, E. Lowering the Detection Limit of Solvent Polymeric Ion-Selective Electrodes. 1. Modeling the Influence of Steady-State Ion Fluxes. *Anal. Chem.* **1999**, *71*, 1204–1209.
- (22) Michalska, A.; Dumańska, J.; Maksymiuk, K. Lowering the Detection Limit of Ion-Selective Plastic Membrane Electrodes with Conducting Polymer Solid Contact and Conducting Polymer Potentiometric Sensors. *Anal. Chem.* **2003**, *75*, 4964–4974.
- (23) Long, R.; Bakker, E. Spectral Imaging and Electrochemical Study on the Response Mechanism of Ionophore-Based Polymeric Membrane Amperometric PH Sensors. *Electroanalysis* **2003**, *15*, 1261–1269.
- (24) Zhang, J.; Harris, A. R.; Cattrall, R. W.; Bond, A. M. Voltammetric Ion-Selective Electrodes for the Selective Determination of Cations and Anions. *Anal. Chem.* **2010**, *82*, 1624–1633.
- (25) Kim, Y.; Amemiya, S. Stripping Analysis of Nanomolar Perchlorate in Drinking Water with a Voltammetric Ion-Selective Electrode Based on Thin-Layer Liquid Membrane. *Anal. Chem.* **2008**, *80*, 6056–6065.
- (26) Cano, M.; Palenzuela, B.; Rodríguez-Amaro, R. A TTF-TCNQ Electrode as a Voltammetric Analogue of an Ion-Selective Electrode. *Electroanalysis* **2006**, *18*, 1068–1074.
- (27) Kraikaew, P.; Sailapu, S. K.; Bakker, E. Rapid Constant Potential Capacitive Measurements with Solid-Contact Ion-Selective Electrodes Coupled to Electronic Capacitor. *Anal. Chem.* **2020**, *92*, 14174–14180.
- (28) Kondratyeva, Y. O.; Tolstopjatova, E. G.; Kirsanov, D. O.; Mikhelson, K. N. Chronoamperometric and Coulometric Analysis with Ionophore-Based Ion-Selective Electrodes: A Modified Theory and the Potassium Ion Assay in Serum Samples. *Sens. Actuators, B* **2020**, *310*, 127894.
- (29) Lisak, G.; Sokalski, T.; Bobacka, J.; Harju, L.; Mikhelson, K.; Lewenstam, A. Tuned Galvanostatic Polarization of Solid-State Lead-Selective Electrodes for Lowering of the Detection Limit. *Anal. Chim. Acta* **2011**, *707*, 1–6.
- (30) Shvarev, A.; Bakker, E. Response Characteristics of a Reversible Electrochemical Sensor for the Polyion Protamine. *Anal. Chem.* **2005**, *77*, 5221–5228.
- (31) Shvarev, A.; Bakker, E. Pulsed Galvanostatic Control of Ionophore-Based Polymeric Ion Sensors. *Anal. Chem.* **2003**, *75*, 4541–4550.
- (32) Perera, H.; Fordyce, K.; Shvarev, A. Pulsed Galvanostatic Control of Solid-State Polymeric Ion-Selective Electrodes. *Anal. Chem.* **2007**, *79*, 4564–4573.
- (33) Kugimiya, A.; Takei, H. Preparation of Molecularly Imprinted Polymers with Thiourea Group for Phosphate. *Anal. Chim. Acta* **2006**, *564*, 179–183.
- (34) Alahi, M. E. E.; Mukhopadhyay, S. C.; Burkitt, L. Imprinted Polymer Coated Impedimetric Nitrate Sensor for Real-Time Water Quality Monitoring. *Sens. Actuators, B* **2018**, *259*, 753–761.
- (35) Morf, W. E. *The Principles of Ion-Selective Electrodes and of Membrane Transport*; Elsevier, 2012.
- (36) Bard, A. J.; Faulkner, L. R.; et al. Fundamentals and Applications: Electrochemical Methods. *Electrochem. Methods* **2001**, *2*, 580–632.
- (37) Bühlmann, P.; Umezawa, Y. Apparently “Non-Nernstian” Equilibrium Responses Based on Complexation Between the Primary Ion and a Secondary Ion in the Liquid ISE Membrane. *Electroanalysis* **1999**, *11*, 687–693.

- (38) Koryta, J.; Stulik, K. Ion-Selective Electrodes. *Annu. Rev. Mater. Sci.* **1986**, *16*, 13–27.
- (39) Zook, J. M.; Buck, R. P.; Langmaier, J.; Lindner, E. Mathematical Model of Current-Polarized Ionophore-Based Ion-Selective Membranes. *J. Phys. Chem. B* **2008**, *112*, 2008–2015.
- (40) Liu, S.; Ding, J.; Qin, W. Current Pulse Based Ion-Selective Electrodes for Chronopotentiometric Determination of Calcium in Seawater. *Anal. Chim. Acta* **2018**, *1031*, 67–74.
- (41) Sarveiya, V.; Templeton, J. F.; Benson, H. A. E. Effect of Lipophilic Counter-Ions on Membrane Diffusion of Benzydamine. *Eur. J. Pharm. Sci.* **2005**, *26*, 39–46.
- (42) Ding, J.; Wang, X.; Qin, W. Pulsed Galvanostatic Control of a Polymeric Membrane Ion-Selective Electrode for Potentiometric Immunoassays. *ACS Appl. Mater. Interfaces* **2013**, *5*, 9488–9493.
- (43) Gettler, R. C.; Alaál, N.; Brorsen, K. R.; Young, M. J. Effects of Interchain Crosslinking by Alkyl Dihalides on the Electrochemical Performance of Nanoscale Polypyrrole Films. *Chem. Mater.* **2022**, *34*, 8065–8076.
- (44) López Cascales, J. J.; Otero, T. F. Molecular Dynamic Simulation of the Hydration and Diffusion of Chloride Ions from Bulk Water to Polypyrrole Matrix. *J. Chem. Phys.* **2004**, *120*, 1951–1957.
- (45) Christoffels, L. A. J.; de Jong, F.; Reinhoudt, D. N. Facilitated Transport of Salts by Neutral Anion Carriers. *Chem.–Eur. J.* **2000**, *6*, 1376–1385.
- (46) Pahlavanzadeh, H.; Katal, R.; Mohammadi, H. Synthesize of Polypyrrole Nanocomposite and Its Application for Nitrate Removal from Aqueous Solution. *J. Ind. Eng. Chem.* **2012**, *18*, 948–956.
- (47) Ye, Q.; Borbély, S.; Horvai, G. Microstructure of Ion-Selective Plasticized PVC Membranes Studied by Small-Angle Neutron Scattering. *Anal. Chem.* **1999**, *71*, 4313–4320.
- (48) Cheong, Y. H.; Ge, L.; Lisak, G. Highly Reproducible Solid Contact Ion Selective Electrodes: Emerging Opportunities for Potentiometry - A Review. *Anal. Chim. Acta* **2021**, *1162*, 338304.
- (49) Han, T.; Kalinichev, A. V.; Mousavi, Z.; Mikhelson, K. N.; Bobacka, J. Anomalous Potentiometric Response of Solid-Contact Ion-Selective Electrodes with Thin-Layer Membranes. *Sens. Actuators, B* **2022**, *357*, 131416.
- (50) Hu, J.; Stein, A.; Bühlmann, P. Rational Design of All-Solid-State Ion-Selective Electrodes and Reference Electrodes. *TrAC, Trends Anal. Chem.* **2016**, *76*, 102–114.
- (51) Pankratova, N.; Ghahraman Afshar, M.; Yuan, D.; Crespo, G. A.; Bakker, E. Local Acidification of Membrane Surfaces for Potentiometric Sensing of Anions in Environmental Samples. *ACS Sens* **2016**, *1*, 48–54.
- (52) Wang, N.; Ivey, C. D.; Dorman, R. A.; Ingersoll, C. G.; Steevens, J.; Hammer, E. J.; Bauer, C. R.; Mount, D. R. Acute Toxicity of Sodium Chloride and Potassium Chloride to a Unionid Mussel (*Lampsilis Siliquoides*) in Water Exposures. *Environ. Toxicol. Chem.* **2018**, *37*, 3041–3049.
- (53) Serrano-Nascimento, C.; Nunes, M. T. Perchlorate, Nitrate, and Thiocyanate: Environmental Relevant NIS-Inhibitors Pollutants and Their Impact on Thyroid Function and Human Health. *Front. Endocrinol.* **2022**, *13*.
- (54) Gemene, K. L.; Shvarev, A.; Bakker, E. Selectivity Enhancement of Anion-Responsive Electrodes by Pulsed Chronopotentiometry. *Anal. Chim. Acta* **2007**, *583*, 190–196.
- (55) Marcus, Y. Thermodynamics of Solvation of Ions. Part 5.—Gibbs Free Energy of Hydration at 298.15 K. *J. Chem. Soc., Faraday Trans.* **1991**, *87*, 2995–2999.
- (56) Davies, J. E. W.; Moody, G. J.; Thomas, J. D. R. Nitrate Ion Selective Electrodes Based on Poly(Vinyl Chloride) Matrix Membranes. *Analyst* **1972**, *97*, 87.
- (57) Garcia-Cruz, A.; Ahmad, O. S.; Alanazi, K.; Piletska, E.; Piletsky, S. A. Generic Sensor Platform Based on Electro-Responsive Molecularly Imprinted Polymer Nanoparticles (e-NanoMIPs). *Microsyst. Nanoeng.* **2020**, *6*, 83.
- (58) BelBruno, J. J. Molecularly Imprinted Polymers. *Chem. Rev.* **2019**, *119*, 94–119.
- (59) Haupt, K.; Mosbach, K. Molecularly Imprinted Polymers and Their Use in Biomimetic Sensors. *Chem. Rev.* **2000**, *100*, 2495–2504.
- (60) Caldara, M.; van Wissen, G.; Cleij, T. J.; Diliën, H.; van Grinsven, B.; Eersels, K.; Lowdon, J. W. Deposition Methods for the Integration of Molecularly Imprinted Polymers (MIPs) in Sensor Applications. *Adv. Sens. Res.* **2023**, *2*.
- (61) Wyatt, Q. K.; Vaninger, M.; Paranamana, N. C.; Heitmann, T. W.; Kaiser, H.; Young, M. J. Oxidative Molecular Layer Deposition of Amine-Containing Conjugated Polymer Thin Films. *ACS Appl. Polym. Mater.* **2022**, *4*, 6156–6168.
- (62) Wyatt, Q. K.; Brathwaite, K. G.; Ardiansyah, M.; Paranamana, N. C.; Brorsen, K. R.; Young, M. J. Mechanistic Insights into Oxidative Molecular Layer Deposition of Conjugated Polymers. *Chem. Mater.* **2023**, *35*, 154–162.
- (63) Gettler, R. C.; Kinlen, P. J.; Renfroe, E.; Xing, Y.; Young, M. J. Postprocessing of Solution-Cast Polyaniline for Enhanced Electrochemical Properties. *J. Power Sources* **2023**, *583*, 233557.
- (64) Sotoudeh, M.; Groß, A. Descriptor and Scaling Relations for Ion Mobility in Crystalline Solids. *JACS Au* **2022**, *2*, 463–471.
- (65) Rollings, R. C.; Kuan, A. T.; Golovchenko, J. A. Ion Selectivity of Graphene Nanopores. *Nat. Commun.* **2016**, *7*, 11408.
- (66) Balme, S.; Picaud, F.; Manghi, M.; Palmeri, J.; Bechelany, M.; Cabello-Aguilar, S.; Abou-Chaaya, A.; Miele, P.; Balanzat, E.; Janot, J. M. Ionic Transport through Sub-10 Nm Diameter Hydrophobic High-Aspect Ratio Nanopores: Experiment, Theory and Simulation. *Sci. Rep.* **2015**, *5*, 10135.
- (67) Xue, L.; Yamazaki, H.; Ren, R.; Wanunu, M.; Ivanov, A. P.; Edel, J. B. Solid-State Nanopore Sensors. *Nat. Rev. Mater.* **2020**, *5*, 931–951.
- (68) Lai, M.; Obliger, A.; Lu, D.; Kley, C. S.; Bischak, C. G.; Kong, Q.; Lei, T.; Dou, L.; Ginsberg, N. S.; Limmer, D. T.; Yang, P. Intrinsic Anion Diffusivity in Lead Halide Perovskites Is Facilitated by a Soft Lattice. *Proc. Natl. Acad. Sci. U.S.A.* **2018**, *115*, 11929–11934.